

The development of a finite element model for ballistic impact predictions

By

Richard Allen Perkins

Approved by:

Yucheng Liu (Major Professor)
Youssef Hammi (Co-Major Professor)
Raj Prabhu (Committee Member)
Tonya Stone (Graduate Coordinator)
Jason M. Keith (Dean, Bagley College of Engineering)

A Thesis
Submitted to the Faculty of
Mississippi State University
in Partial Fulfillment of the Requirements
for the Degree of Master of Science
in Mechanical Engineering
in the Bagley College of Engineering

Mississippi State, Mississippi

December 2021

DISTRIBUTION A. Approved for public release; distribution unlimited. OPSEC #: 5486

Copyright by
Richard Allen Perkins
2021

Name: Richard Allen Perkins

Date of Degree: December 10, 2021

Institution: Mississippi State University

Major Field: Mechanical Engineering

Major Professors: Yucheng Liu, Youssef Hammi

Title of Study: The development of a finite element model for ballistic impact predictions

Pages in Study: 41

Candidate for Degree of Master of Science

Concrete is a widely used product and is an important application throughout industry due to its inexpensive cost and wide range of applications. This work focuses on understanding the behavior of high strength concrete in high strain rate ballistic impact loading scenarios. A finite element analysis was created with the implementation of the Concrete Damage and Plasticity Model 2 (CDPM2) to represent the material behavior. The model's parameters were calibrated to existing literature and the results were analyzed by a comparison of the impact velocity to residual velocity and a qualitative assessment of the impact crater. The model captured the impact dynamics of the contact between the projectile and the concrete target with defined fracture patterns. Impact velocity and target thickness indicated a relatively linear relationship with the final projectile velocity.

ACKNOWLEDGEMENTS

I would like to take this opportunity to expressive my gratitude to all those who have supported me during my master's program. First, I would like to thank my Lord and savior Jesus Christ for enabling the completion of my research and my degree. I would like to also thank my advisor Dr. Youssef Hammi and my committee members Dr. Raj Prabhu and Dr. Yucheng Liu for their support and guidance throughout my research. Finally, I would like to thank the Engineer Research and Development Center (ERDC) and the Center For Advanced Vehicular Systems (CAVS) for funding my research.

TABLE OF CONTENTS

ACKNOWLEDGEMENTS	ii
LIST OF TABLES	iv
LIST OF FIGURES	v
CHAPTER	
I. HIGH STRENGTH CONCRETE AND FIBER REINFORCEMENT	1
1.1 High Strength Concrete and Fiber Reinforcement	1
1.2 Ballistic Impact Loadings	3
1.3 Computational modeling of cementitious materials and equation of states	6
II. CDPM2 CONCRETE MATERIAL MODEL FORMULATION	10
III. CDPM2 MATERIAL CALIBRATION FOR BBR9 CONCRETE	16
3.1 CDPM2 Model Constants	16
3.2 BBR9 Calibration	17
IV. BBR9 IMPACT SIMULATIONS USING CDPM2 MATERIAL MODEL FORMULATION	20
4.1 Mesh Convergence Study of Finite Element Model	20
4.2 Finite Element Simulation Design	22
4.3 Finite Element Simulation Results	23
V. DISCUSSION OF FINITE ELEMENT SIMULATION RESULTS AND FUTURE WORK	28
5.1 Concrete Target Fragmentation Process	28
5.2 Limitations of Finite Element Model and Future Work	32
VI. CONCLUSION	34
REFERENCES	36

LIST OF TABLES

Table 3.1 CDPM2 model parameters for BBR9 Concrete used in the analysis.....19

LIST OF FIGURES

Figure 1.1	Comparison of UHPC with and without fibers (Leutbecher, n.d.).....	2
Figure 1.2	Impact Experiments of Concrete with (left) and without (right) fiber reinforcement (Pontiroli, 2019).....	3
Figure 1.3	Relationship between the compressive strength of concrete and the influence of its strain rate (Bischoff and Perry, 1991).	4
Figure 1.4	Failure process in ballistic impact of concrete structures (Pereira et al., 2018a).	5
Figure 1.5	Flow chart for the full subroutine found in (Martineau, 1998).	8
Figure 2.1	Influence of the hardening laws q_{h1} and q_{h2} in conjugation with the Hardening Parameter H_p (Grassl et al., 2013).	12
Figure 2.2	Bi-Linear softening law used to determine the softening in tension (Grassl et al., 2018).	14
Figure 2.3	Exponential softening law used for the representation of softening in compression (Grassl et al., 2018).	15
Figure 3.1	BBR9 calibration results of comparison between single element and experimental triaxial compression with various confinement levels.	18
Figure 4.1	Finite element target used for the projectile impact simulations.....	20
Figure 4.2	Results of mesh convergence study from the projectile impact simulations.....	21
Figure 4.3	Results of the target in the mesh convergence studies.	22
Figure 4.4	Comparison of the initial velocities versus the residual velocities for the BBR9 concrete using CDPM2 for a target with a thickness of 1 in.....	24
Figure 4.5	Comparison of the residual velocity to different target thickness for three different impact velocities.	25

Figure 4.6 Effect of the target thickness on crater size for the projectile impact with an initial velocity of 1000ms^{-1} 26

Figure 4.7 Effect of the projectile diameter on the residual velocity for a ballistic impact at 1000ms^{-1} and a target with a thickness of 1 in.27

Figure 5.1 Pressure contour showing the stress wave propagation through the cross section of the target for a ballistic impact of a 1 in target and a 1000ms^{-1} initial velocity.....29

Figure 5.2 Aspects of the ballistic impact seen throughout the target of a ballistic impact simulation with an initial velocity of 1000ms^{-1} and target thickness of 1 in.....30

Figure 5.3 Resulting scabbing and tunnel diameters from a ballistic impact with an initial velocity of 1000ms^{-1} and target thickness of 1 in.31

CHAPTER I
HIGH STRENGTH CONCRETE AND FIBER REINFORCEMENT

1.1 High Strength Concrete and Fiber Reinforcement

There is a growing interest by researchers to study concrete materials due to its wide range of applications and cost-efficient nature. Concrete is commonly employed in construction design for structures such as buildings or bridges as it is the most commonly used material in construction (Knoeri et al., 2013). Concrete is known to exhibit brittle material qualities and therefore can withstand high compressive stress but is inferior under tensile loading. Significant research interest has been invested in determining methods to improve the strength of concrete and furthermore the applicability of the material. This led to the eventual development of high strength concrete, high performance concrete (HPC), fiber reinforced concrete, and Ultra-High-Performance Concrete (UHPC). Concrete with compressive strengths that exceed 150 MPa are designated as UHPC (Russell and Graybeal, 2013). This concrete achieves its high performance through a low water to binder ratio (w/b) such that the porosity of the matrix of the concrete is decreased (Wille et al., n.d.), which also enables this concrete to have a high durability (Alkaysi et al., 2016). This concrete is typically more expensive than regular types of concrete; however, the increase in strength enables less material to be used in designs which will reduce the overall cost. UHPC has also been designed with steel fiber reinforcement to further improve its mechanical strength producing a type of concrete denoted as Ultra High Performance Fiber Reinforced Concrete (UHPFRC) (Song and Hwang, 2004). UHPFRC is known to have

compressive and tensile strengths as high as 200MPa and 40MPa respectively (Mao et al., 2014). The fibers have been shown to greatly improve the mechanical behavior of the concrete. This improvement is highlighted by the typical stress and strain diagrams as seen in Figure 1.1.

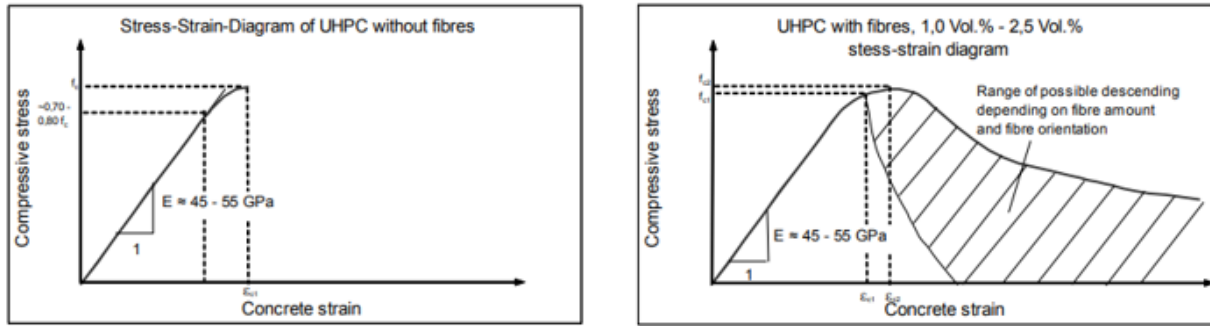


Figure 1.1 Comparison of UHPC with and without fibers (Leutbecher, n.d.).

The shape of the fiber that is introduced to the concrete mix such as straight, hooked, or twisted ends have also been shown to effect the performance of the resulting concrete mix (Yoo and Banthia, 2016). Additional factors such as the amount of fiber has been studied as well to seek methods to improve the performance of cementitious mixtures. The effects of fibers become apparent in projectile impact experiments. When concrete without fibers is struck with a high-speed projectile the concrete target exhibits a greater brittle fragmentation than a target with the fibers. This is demonstrated by the experimental results shown in Figure 1.2.



Figure 1.2 Impact Experiments of Concrete with (left) and without (right) fiber reinforcement (Pontiroli, 2019)

These improvements in concrete further lead to the growing interest by researchers in high performance concrete.

1.2 Ballistic Impact Loadings

The behavior of concrete has been demonstrated to be highly dependent on the applied strain rate during loading scenarios. It has been widely reported that the strength of concrete is improved as the strain rate increases. This is apparent as both the compressive and tensile strength of the material increases under higher strain rate loading scenarios (Grote et al., 2001; Soroushian et al., 1985). This lead to the conclusion that the dynamic strength of concrete is much higher than its static strength (Mainstone, 1975). This created a strong interest in understanding the behavior of concrete in ballistic impact scenarios, as blast impacts are commonly reported to experience strain rates as high as 10^2 and 10^3 s^{-1} . The relationship between the strain rate and increase in compressive strength can be seen in Figure 1.3. Some authors have

reported an increase in a concrete's compressive strength between 200% and 400% at these strain rates when it is compared to a static loading situation (Bischoff and Perry, 1991).

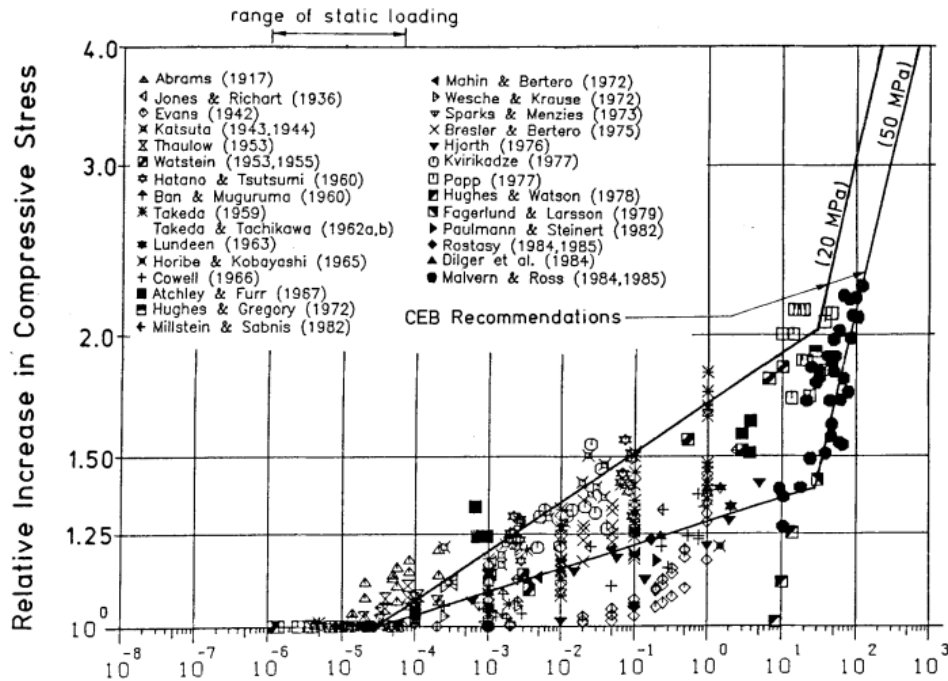


Figure 1.3 Relationship between the compressive strength of concrete and the influence of its strain rate (Bischoff and Perry, 1991).

Continued research on this subject lead to the conclusion that this phenomenon was due to inertial confinement produced by the high strain rates instead of a material characteristic. This was shown through Split Hopkinson Pressure Bar (SHPB) experiments of concrete (Li and Meng, 2003) (Zhang et al., 2009). This placed an increased emphasis on evaluating the mechanical properties of concrete at lower strain rates to determine its characteristic strength properties (Chen et al., 2013). Many researchers have investigated ballistic impact scenarios in an effort to understand this complex process. Several empirical formulas have been developed to

predict important results due to the ballistic impact such as the projectile penetration depth or fragmentation penetration depth based on available material data (Li et al., 2005). Throughout the impact scenario the structure is exposed to shock waves that create a multiaxial stress state throughout the material leading to a complex failure process. Additionally, the porous nature of concrete causes the unique failure process due to the crushing of the voids throughout the material. This failure process in its entirety is defined in (Pereira et al., 2018a) as five key stages which can be visualized in Figure 1.4.

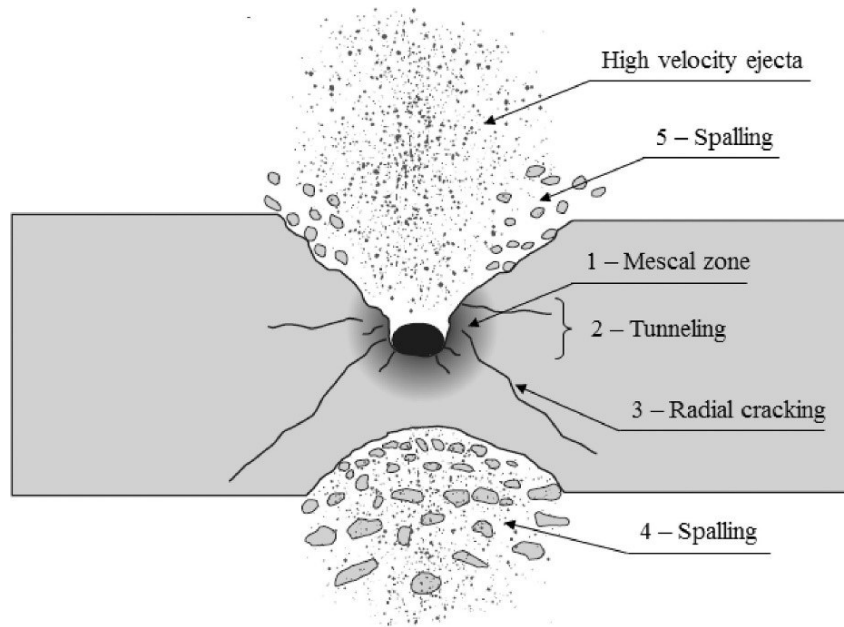


Figure 1.4 Failure process in ballistic impact of concrete structures (Pereira et al., 2018a).

The first stage in this process is the Mescal Zone. This is caused by the crushing and compaction of the material at the strike face, which will then cause the tunneling of this crushed material. The lateral pressure resulting from the initial shock wave creates radial crack propagation

out from the strike face. The spalling is a result of the initial compression wave transforming into a tensile wave at the free boundary to cause the ejection of the material. The majority of the fragments will originate from the impact site with any fragmentation occurring away from the impact site occurring due the reflection of the stress waves (Woodward et al., 1991). Experimental evidence also shows the spall area on the back surface of a target to be larger than area on the front due to this behavior (Beppu et al., 2008).

1.3 Computational modeling of cementitious materials and equation of states

The common implementation and wide range of applications that concrete is employed for has produced a strong desire to accurately predict its behavior using computational models. The finite element method (FEM) is a common method that has been used for this purpose with several models which have been developed. Additionally, the finite element method has been shown to successfully model high strain rate impacts for many types of applications such as impacts in metallic materials or structural damage scenarios (Dou et al., 2016, 2020; He et al., 2018a; Liu et al., 2011, 2015a, 2015b; Liu and Day, 2006, 2008). Plasticity models have been developed to estimate the nature of this material through the definition of a yield function, flow rule, and hardening/softening functions. One such type is the Drucker-Prager model (Drucker and Prager, 1952). This model is considered to be a rather simple plasticity model but has been shown to accurately model the performance of concrete once the parameters have been defined (Jiang and Wu, 2012; Yu et al., 2010). Of particular interest is the effect of high strain rate loading scenarios for concrete materials in cases such as ballistic impact, explosive detonations, or blast loadings. Several authors have implemented finite element analysis for predictions of fiber reinforced composites undergoing a high strain rate loading state (Ge He et al., 2017; G He

et al., 2017; He et al., 2021, 2020, 2019b, 2019a, 2018b, p.; He and Liu, 2019). As mentioned previously, concrete is known to highly exhibit strain rate dependent behavior. Previous models must be adjusted to ensure it correctly captures the nature of concrete at these higher strain rates. This is commonly represented using a Mie Gruneisen equation of state which is frequently used when modeling materials at high pressure. This equation of state enables the pressure to be related to the energy and density of a material. Therefore, it is commonly used when modeling ballistic impact or detonation experiments. This equation of state is expressed by equation 1.1 where U_s and U_p are the shock and projectile velocities respectively. The variables C_0 and s define the slope of the shock and projectile velocity curve (“ABAQUS: Theory Manual, Version 6.6,” 2009).

$$U_s = C_0 + sU_p \quad (1.1)$$

Several authors have implemented this equation of state to accurately represent these types of loadings. Hugoniot properties can be determined to define the model parameters used to represent this material behavior. Most commonly, this is accomplished by using shock compression tests to relate the projectile and shock velocities of the experiment (Katayama et al., 2017). In (Martineau, 1998) Martineau developed a model to incorporate the equation of state to better predict the behavior of materials during high pressure explosive detonations, which would cause the material to behave differently as when compared to lower strain rate loadings. This numerical model is implemented using a VUMAT subroutine which is built through an array of multiple subroutines. These subroutines work in conjunction to define the specified modules for

this model and are implemented in an incremental fashion. This is most clearly seen by the flow chart shown in Figure 1.5.

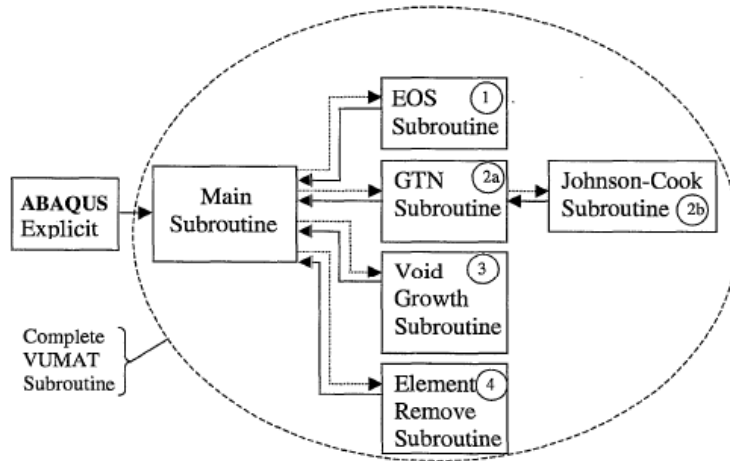


Figure 1.5 Flow chart for the full subroutine found in (Martineau, 1998).

Another challenge in modeling concrete is accounting for the porous nature of concrete. One model that has been proposed is the P- α equation of state model which is designed to define the compaction of porous materials. This model is commonly governed by the Mie Gruneisen equation of state and allows the pressure to be described with relation to the porosity of the material. This equation of state describes the pressure with respect to three variables: α , the density, and the internal energy per unit mass. The scalar variable α , is used to define the porosity of the material as seen in equation 1.2 where ρ_s is the density of the solid material and ρ is the density of the porous material.

$$\alpha = \frac{\rho_s}{\rho} \tag{1.2}$$

A material that is fully compacted is represented when α equals a value of one. Luccioni et. al incorporated this equation of state in their studies of high strength fiber reinforced concrete slabs. They used this equation of state in conjunction with the RHT concrete model to define the material behavior of the concrete they were studying. Several different types of detonation experiments were conducted and then compared to numerical simulations. Upon evaluation of the results, good agreement could be seen between the experiments and the numerical data. The model was shown to agree well with the experimental data for the overpressure evaluation through one of the experiments that was conducted (Luccioni et al., 2018). In (Gebbeken and Hartmann, 2010), the Mie Gruneisen and p - α equation of state parameters were used to model cement stone. Their model was compared to experimental data and showed good agreement. The pressure was evaluated as a function of density and the model closely resembled their experimental results. Additionally, this equation of state has been incorporated into models to describe the behavior of steel reinforced high strength concrete under high strain rate loading. It was used to describe the porous nature of the concrete model and numerical simulations of the explosion of a concrete slab were correlated to experimental data. The simulations implemented a coupled Eulerian-Lagrangian approach for the interaction between the concrete slab and the explosion. The damage of the slab was correlated to experimental data and good agreement between the results could be seen (Yun and Park, 2013).

CHAPTER II

CDPM2 CONCRETE MATERIAL MODEL FORMULATION

Continued progression in plasticity models lead to the development of coupled plasticity and damage models to further replicate the behavior of concrete and its fracture mechanics. The Concrete Damage Plasticity Model 1 (CDPM1) is a plasticity and damage model that involves a pre-damage stress-based plasticity formulation along with a strain-based damage formulation. This model has been shown to closely replicate a wide array of experimental data featuring multiaxial stress states (Grassl and Jirásek, 2006). This initial model was refined to improve the representation of the conversion of tensile to compressive failure and the mesh independency in the Concrete Damage Plasticity Model 2 (CDPM2). CDPM1 used a single damage variable that was expanded to two in CDPM2 by including separate isotropic damage variables for both tension and compression. This improved the response of the model to capture the failure processes of concrete more realistically. To improve the mesh independency of the perfect-plastic response in the CDPM1, hardening was improved to include the formulation for the hardening in the post-peak regime in CDPM2 (Grassl et al., 2013). This model has shown good agreement with experimental testing and the prediction of various failure mechanisms (Seok et al., 2020). Since this model has shown to represent the behavior of concrete well it has been used in several studies. For instance, it has been shown to capture the failure of reinforced concrete and represent the behavior of concrete at high strain rates due to an explosive detonation (Grassl et al., 2018; Hai and Ren, 2020).

An overview of this model is provided in this section based on the authors' work as previously mentioned. The CDPM2 model's formulation is fundamentally derived from the stress-strain relationship presented in equation 2.1.

$$\boldsymbol{\sigma} = (1 - \omega_t) \bar{\boldsymbol{\sigma}}_t + (1 - \omega_c) \bar{\boldsymbol{\sigma}}_c \quad (2.1)$$

In this relationship the positive and negative parts of the effective stress tensor ($\bar{\boldsymbol{\sigma}}$) are represented by $\bar{\boldsymbol{\sigma}}_t$ and $\bar{\boldsymbol{\sigma}}_c$ respectively. Furthermore, this relationship differentiates the different damage variables for tension and compression as previously mentioned by ω_t and ω_c . These definitions improved the model's ability to represent failure in a more realistic manner. The plasticity part of the model is not influenced by the damage since it is only controlled by the effective stress. This results in the strength envelope being controlled by the plasticity part and the representation of damage will begin in the softening region. The yield function is controlled by the effective stress state and the hardening variable κ_p . The hardening variable is further influenced by two hardening laws q_{h1} and q_{h2} . These laws enable the yield function to be defined by the relationship in equation 2.2 where $\bar{\theta}$ is the lode angle, $\bar{\sigma}_v$ is the volumetric effect stress, and $\bar{\rho}$ is the norm of the deviatoric effective stress.

$$f(\bar{\boldsymbol{\sigma}}, \kappa_p) = F(\bar{\sigma}_v, \bar{\rho}, \bar{\theta}, q_{h1}, q_{h2}) \quad (2.2)$$

The incorporation of both hardening laws signifies an improvement upon the original CDPM model. By including two hardening formulations and the hardening parameter (H_p), the

hardening will continue beyond the peak regime. The influence of these two hardening laws and the hardening parameter is best seen by Figure 2.1.

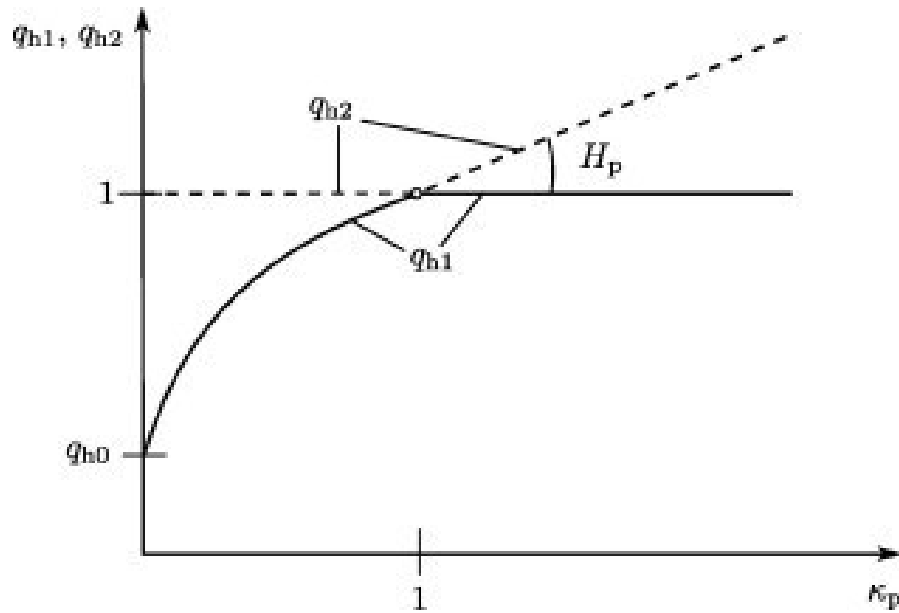


Figure 2.1 Influence of the hardening laws q_{h1} and q_{h2} in conjunction with the Hardening Parameter H_p (Grassl et al., 2013).

The hardening parameter controls the degree of hardening in the post-peak regime with higher values correlating to a lesser degree of plasticity in the model's response. If the q_{h2} hardening law produces a value of one, there will be no contribution of material hardening beyond the peak regime. The evolution of the first hardening law is defined as a function of the hardening parameter by equation 2.3 where q_{h0} is defined as the ratio of the compressive strength when the initial yield limit is reached to the compressive strength of the concrete.

$$q_{h1}(\kappa_p) = \begin{cases} q_{h0} + (1 - q_{h0})(\kappa_p^3 - 3\kappa_p^2 + 3\kappa_p) - H_p(\kappa_p^3 - 3\kappa_p^2 + 2\kappa_p) & \text{if } \kappa_p < 1 \\ 1 & \text{if } \kappa_p \geq 1 \end{cases} \quad (2.3)$$

Once the hardening variable approaches one, the plastic response is driven by the second hardening law presented in equation 2.4.

$$q_{h2}(\kappa_p) = \begin{cases} 1 & \text{if } \kappa_p < 1 \\ 1 + H_p(\kappa_p - 1) & \text{if } \kappa_p \geq 1 \end{cases} \quad (2.4)$$

As can be seen, this law is strongly influenced by the hardening parameter to update the plastic response in this region. The evolution of the hardening variable is defined according to equation 2.5.

$$\dot{\kappa}_p = H(\bar{\sigma}, \kappa_p) \quad (2.5)$$

This is implemented to define the plastic flow rule used to represent the volumetric expansion during compressive loading. This is defined by equation 2.6 where $\dot{\varepsilon}_p$ represents the rate of plastic strain and $g_p(\bar{\sigma}, \kappa_p)$ is the plastic potential function.

$$\dot{\varepsilon}_p = \lambda \frac{\partial g_p}{\partial \bar{\sigma}}(\bar{\sigma}, \kappa_p) \quad (2.6)$$

The material's softening response is used to formulate the compressive and tensile damage variables. The damage will begin to be accounted for once the threshold of the

maximum equivalent strain reaches f_t/E in the history of the material. The damage variables are determined in the calculation through scalar history variables defined for both compression and tension. There are two softening laws that are used to define the tensile and compressive softening regime. A bilinear softening law is used to determine the tensile softening behavior. This law is defined by two material constants that define the crack opening threshold (ω_f and ω_{f1}) and the stress threshold (f_{t1}) to determine the rate of damage. This law is illustrated by Figure 2.2.

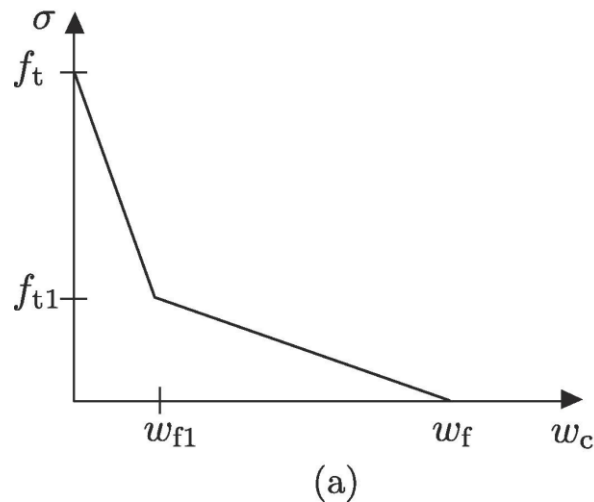


Figure 2.2 Bi-Linear softening law used to determine the softening in tension (Grassl et al., 2018).

The softening during compression is determined by an exponential stress-inelastic strain softening law. A singular material constant is used to define a compressive inelastic strain threshold (ϵ_f). Figure 2.3 displays a graphical representation of this law.

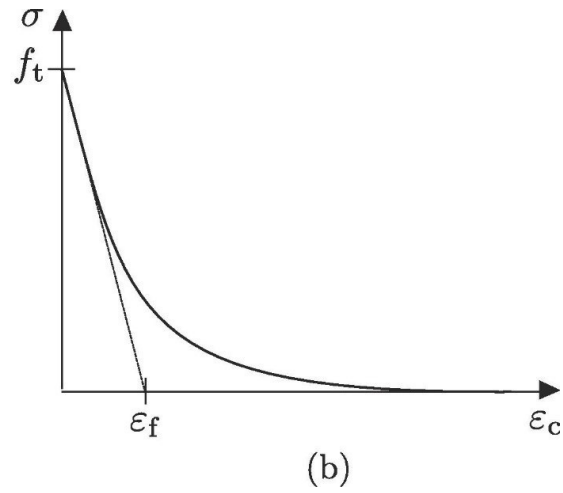


Figure 2.3 Exponential softening law used for the representation of softening in compression (Grassl et al., 2018).

CHAPTER III

CDPM2 MATERIAL CALIBRATION FOR BBR9 CONCRETE

3.1 CDPM2 Model Constants

The CDPM2 material model uses several material constants in its formulation. These parameters can be determined by comparing the model's response to experimental data of uniaxial, biaxial, and triaxial compression tests. Additionally, several of the values have limited effect on the response of the model and can be left as their default value. Finally, some material constants are determined based on provided material properties of the concrete that is considered. The elastic modulus (E), compressive strength (f_c), tensile strength (f_t), and Poisson's ratio (ν) are specified by the material properties of the concrete. The eccentricity (e) is determined by equation 3.1 in terms of the material's tensile strength, compression strength, and equibiaxial compressive strength (f_{bc}), which is defined as $1.16f_c$.

$$e = \frac{1 + \epsilon}{2 - \epsilon}, \quad \text{where } \epsilon = \frac{f_t}{f_{bc}} \frac{f_{bc}^2 - f_c^2}{f_c^2 - f_t^2} \quad (3.1)$$

The initial hardening parameter (q_{h0}) is defined as the ratio of the of the compressive strength at the initial yield limit in uniaxial compression to the material's compressive strength. ω_f is related to the tensile fracture energy (G_{ft}) by equation 3.2 and the default value of ω_{f1} is 15% of ω_f .

$$\omega_f = \frac{G_{ft} * 4.444}{f_t} \quad (3.2)$$

Finally, the stress threshold is defined as 30% of the material's tensile strength. These relationships along with experimental data are used to determine the material constants needed in the CDPM2 model.

3.2 BBR9 Calibration

The type of concrete that was used for the ballistic impact simulations is a high strength concrete denoted as BBR9. It is a self-consolidating concrete with a maximum aggregate size of 4.75mm. Triaxial compression tests were conducted for this concrete in (Williams et al., 2020) and were used for the calibration procedure. Default values of the ductility measure (A_s) the flow rule parameter (D_f), and the initial hardening parameter (q_{h0}) are 15, 0.85, and 0.1 respectively. These values were shown to have minimal effect and were not altered for the BBR9 concrete. When strain rate effects are used in the formulation, the hardening parameter is set to 0.5 and the initial compression strength (f_{c0}) is set to 10MPa. The tensile damage threshold variables were defined according to equation 3.2. Since experimental data of the fracture energy was not available, the relationship presented in the model code [CEB-FIB 2010] could be used. This relationship defines the fracture energy in terms of the compressive strength of the material and is shown by equation 3.3.

$$G_f = 73f_c^{0.18} \quad (3.3)$$

Based off this relationship, the fracture energy for the BBR9 concrete was determined to be 2081J/m^2 , which enabled the bi-linear softening law constants to be calculated. All other variables were calibrated through the comparison of triaxial compression simulations with various levels of confinement using a single element cube with the experimental data presented in the literature. Six confinement pressures were considered consisting of 10MPa, 20MPa, 50MPa, 100MPa, 200MPa, and 300MPa. The result of the calibration procedure is shown by Figure 3.1.

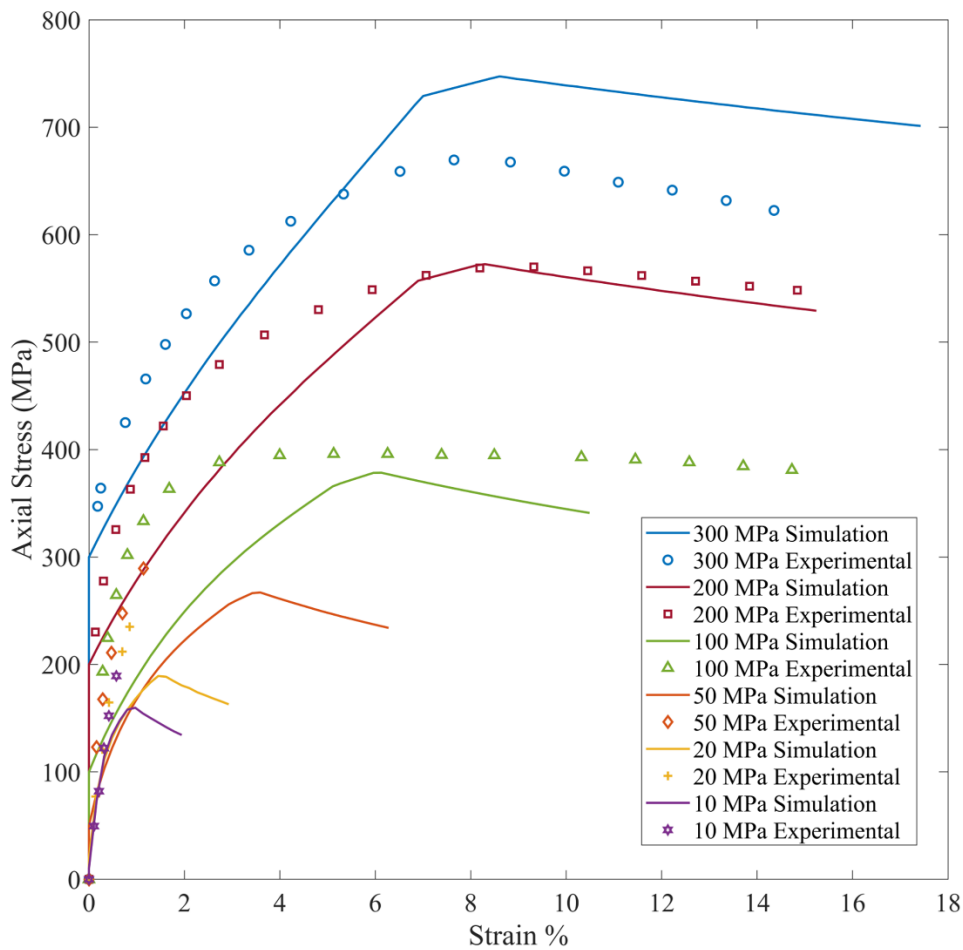


Figure 3.1 BBR9 calibration results of comparison between single element and experimental triaxial compression with various confinement levels.

The calibration results were produced by the determined model parameters for the BBR9 concrete shown in Table 3.1. The model parameters indicated good agreement with the experimental data for the calibration procedure and were used throughout the finite element simulations in this study.

Table 3.1 CDPM2 model parameters for BBR9 Concrete used in the analysis

Model Parameter	Value
Elastic Modulus (E)	40 (GPa)
Poisson's Ratio (ν)	0.15
Eccentricity (e)	0.5126
Initial Hardening Parameter (q_{h0})	0.1
Tensile Strength (f_t)	34 (MPa)
Compressive Strength (f_c)	141.4 (MPa)
Hardening Parameter (H_p)	0.5
Hardening Variable (A_h)	0.145
Hardening Variable (B_h)	0.003
Hardening Variable (C_h)	1.35
Hardening Variable (D_h)	1e-6
Ductility Measure (A_s)	15
Flow Rule Parameter (D_f)	0.85
Initial Compressive Strength (f_{c0})	10 (MPa)
Damage Ductility Measure (b_s)	1.0
Crack Opening Threshold (ω_f)	0.1
Crack Opening Threshold (ω_{f1})	0.01
Stress Threshold (f_{t1})	10.2 (MPa)
Compressive Strain Threshold (ϵ_f)	0.0003
Tension Threshold for Element Deletion (D_{ct})	0.1
Compressive Threshold for Element Deletion (D_{ct})	0.4

CHAPTER IV

BBR9 IMPACT SIMULATIONS USING CDPM2 MATERIAL MODEL FORMULATION

4.1 Mesh Convergence Study of Finite Element Model

To determine the sensitivity of the model to the mesh density of the target, a sensitivity analysis of the number of elements used in the finite element model was conducted. The mesh was refined by increasing the number of elements in the local impact zone of the target. The impact zone was defined by an area of 9in^2 in the center of the target. The finite element target design along with the defined localized impact zone is shown by Figure 4.1.

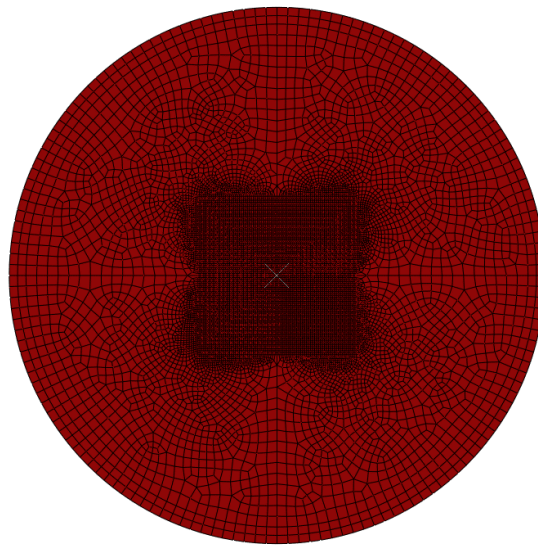


Figure 4.1 Finite element target used for the projectile impact simulations.

The impact zone is represented by the high mesh density region seen at the center of the target.

The target was impacted by a projectile with a 0.25in diameter. The projectile was expected to produce minimal deformation upon impact with the target and was modeled as a rigid body. This is similar to the work by other researchers when simulating a projectile impact in concrete (Li and Tong, 2003) (Bohong, 2004) and was considered an acceptable assumption for this study. The projectile impacted a target with a thickness of 1in at initial velocities of 500ms^{-1} , 800ms^{-1} , and 1000ms^{-1} and the number of elements was increased for the simulations. The primary numerical output used to evaluate ballistic impacts in concrete is the residual velocity; therefore, this output was used to evaluate the mesh. The results of the mesh convergence study are shown by Figure 4.2.

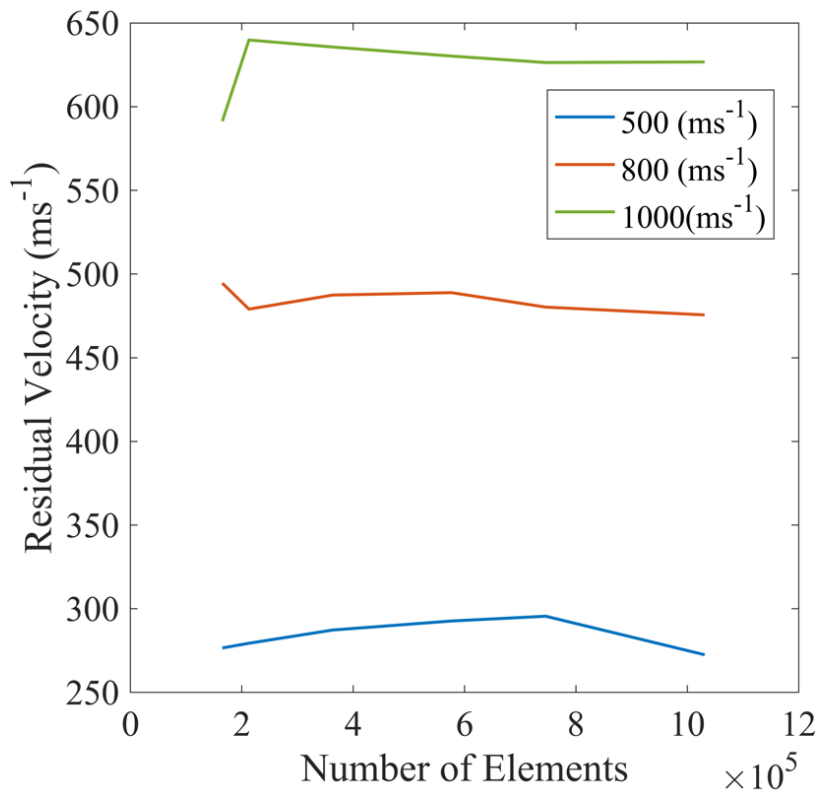


Figure 4.2 Results of mesh convergence study from the projectile impact simulations.

The results of the simulations indicate the material model exhibits a minimal mesh dependency as the maximum difference in the results is under 10%. Additionally, the increase in the number of elements produced the same crater representation as the coarse mesh as can be seen through Figure 4.3.

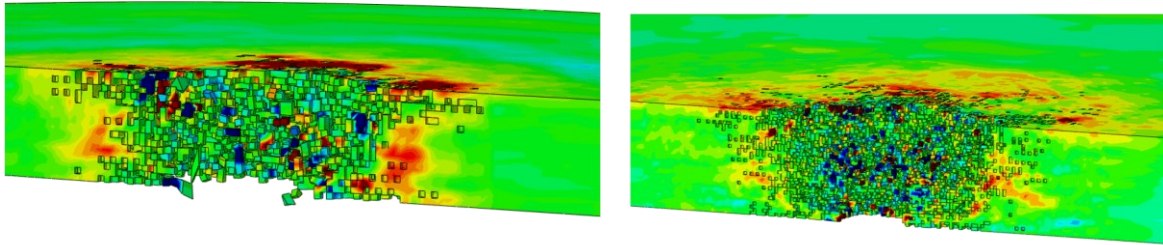


Figure 4.3 Results of the target in the mesh convergence studies.

The mesh density of the impact zone of the target was defined by an average element size of 1.5mm (left) and 0.8mm (right).

It can be seen that the mesh density did not alter the resulting crater from the projectile impacts. Additionally, the reduced mesh sizes improved the computational efficiency of the simulations. Therefore, an average element size of 1.5mm was used for all the simulations in this study since this value limited the computational cost of each simulation and ensured a constant solution in the simulations.

4.2 Finite Element Simulation Design

To test the response of the CDPM2 material model, ballistic impact simulations were designed for the calibrated BBR9 concrete. The purpose of the simulations is to determine the effect of the initial projectile velocity and the thickness of the targets when modeling this loading scenario. The results were evaluated based on a comparison of the residual velocity vs initial

velocity of the projectile, pressure, von mises stress, strain, and the fracture of the target. The range of velocities that were tested ranged from 200ms^{-1} to 1300ms^{-1} and were incremented by 100ms^{-1} for each simulation. This range of velocities has been used throughout literature for ballistic impact experiments (Wu et al., 2019). The target thickness for each of the various velocities was specified as 1in to determine the relationship between the initial projectile velocity and the final projectile velocity. To test the effect of the target thickness, targets with thicknesses of 1in, 1.25in, 1.5in, 1.75in, 2in were implemented in the finite element simulations. Initial velocities of 500ms^{-1} , 800ms^{-1} , and 1000ms^{-1} were prescribed for the projectile for this aspect of the study.

The finite element simulations were completed using the software package Abaqus Explicit (Simulia 2020). The impactor was a spherical projectile with a diameter of 0.25in. The target was dimensioned to be a cylindrical target with a diameter of 406.4mm. 8 node brick elements with reduced integration were used to build the mesh for the target. The total number of elements used in the target's mesh was 273,840. The boundary condition applied to the target consisted of fully fixing the target 1in from its edge in all directions. This simulates the type of casing often used to constrain the targets in ballistic impact experiments. Element deletion was included in the simulations to represent the material fracture.

4.3 Finite Element Simulation Results

The results of the simulations provided an evaluation of the ballistic impact response using the CDPM2 concrete material model calibrated for the high strength BBR9 material. The results of impacting the concrete with the various initial velocities is shown by Figure 4.4.

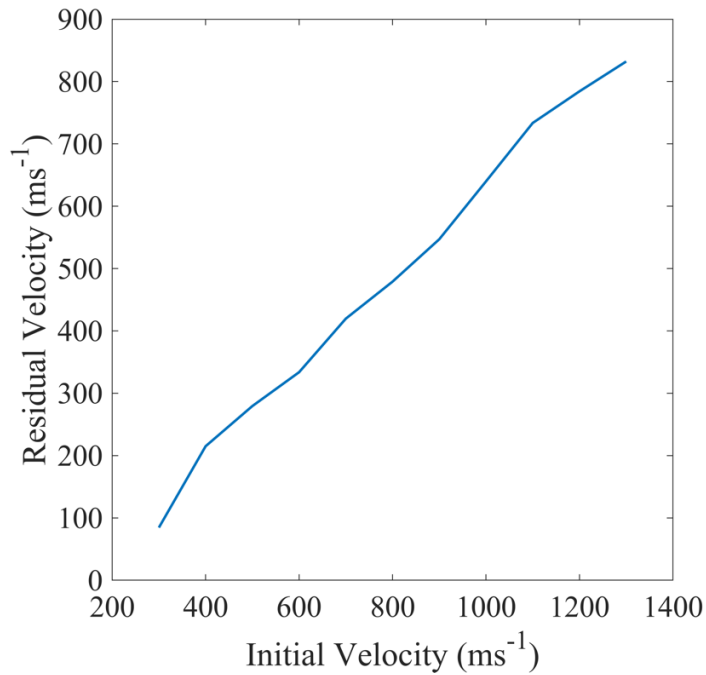


Figure 4.4 Comparison of the initial velocities versus the residual velocities for the BBR9 concrete using CDPM2 for a target with a thickness of 1in.

The relationship between the initial velocity and residual velocity indicates a mostly linear relationship between these variables. Additionally, the damage produced on both the front and rear faces of the concrete increased in proportion with the prescribed initial velocity. At higher impact velocities, the results for the residual velocity are most significantly influenced by the density of the material and less by the strength of the specific concrete. For this reason, an effective evaluation of the CDPM2 concrete model's performance can be conducted by comparing this impact velocity range to experimental data. As previously mentioned, data representing the behavior of the concrete for different thicknesses is of interest in this study. The

results of the impact simulations at different initial velocities and target thicknesses are shown by Figure 4.5.

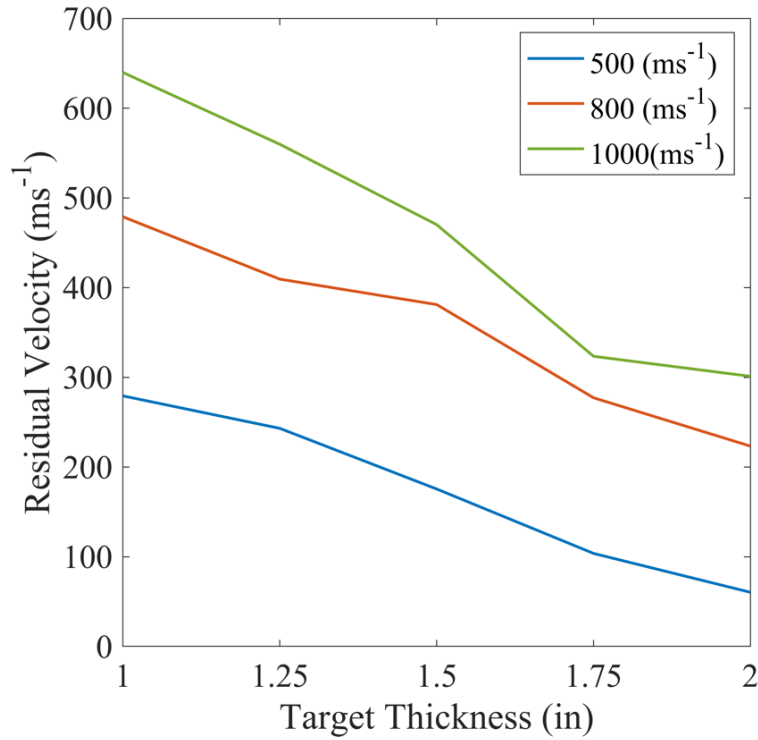


Figure 4.5 Comparison of the residual velocity to different target thickness for three different impact velocities.

The results shown by Figure 4.5 demonstrate a relatively linear relationship between the residual velocity and the target thickness. As expected, the thicker targets produced slower residual velocities in the simulations. Interestingly, there is less of a difference in the residual velocities for target thicknesses of 1.75in and 2in than the other thickness studied as seen by the change in the slope of the line. Like the previous results, the relationship between the target thickness and the residual velocity can be used to evaluate the model with a comparison to

experimental data. The resulting crater predicted through the simulations for an impact velocity of 1000ms^{-1} is shown by Figure 4.6.

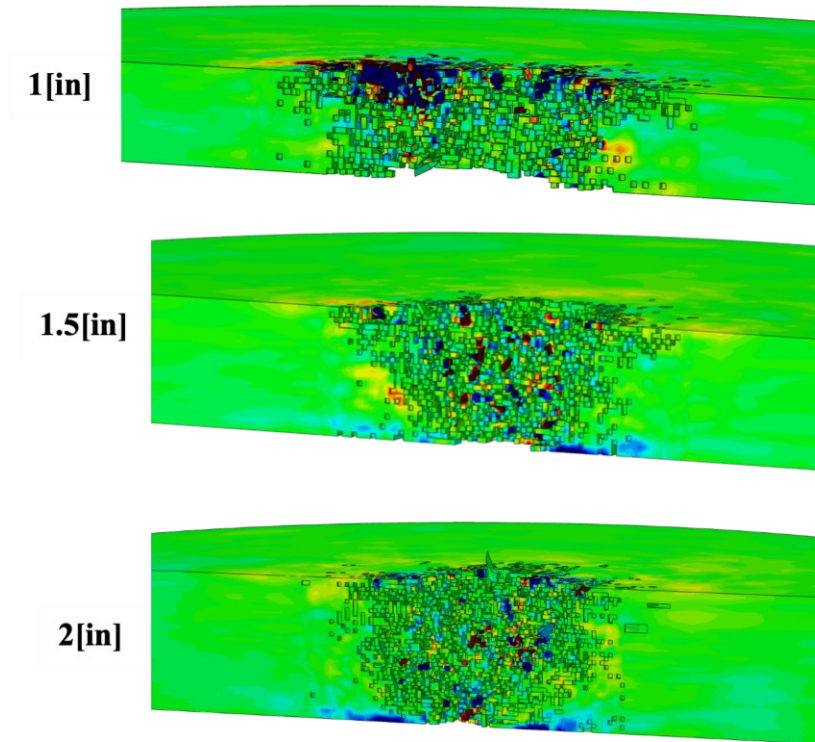


Figure 4.6 Effect of the target thickness on crater size for the projectile impact with an initial velocity of 1000ms^{-1} .

In the simulations the crater size on the rear face reduced in size as the thickness of the target increases. As more material contacted the projectile, the energy applied to the rear face was reduced, which produced the smaller crater size. The crater on the front of the target remained approximately constant. The initial impact site of the target is most heavily influenced by the initial velocity of the projectile. The damage on the front side of the target differed for different initial velocities. Simulations were also performed to consider the influence in the diameter of

the projectile by considering two additional projectile diameters. Projectile diameters of 0.25in, 0.75in, and 1in impacted a 1in target at 1000 ms⁻¹ and the results are shown in Figure 4.7.

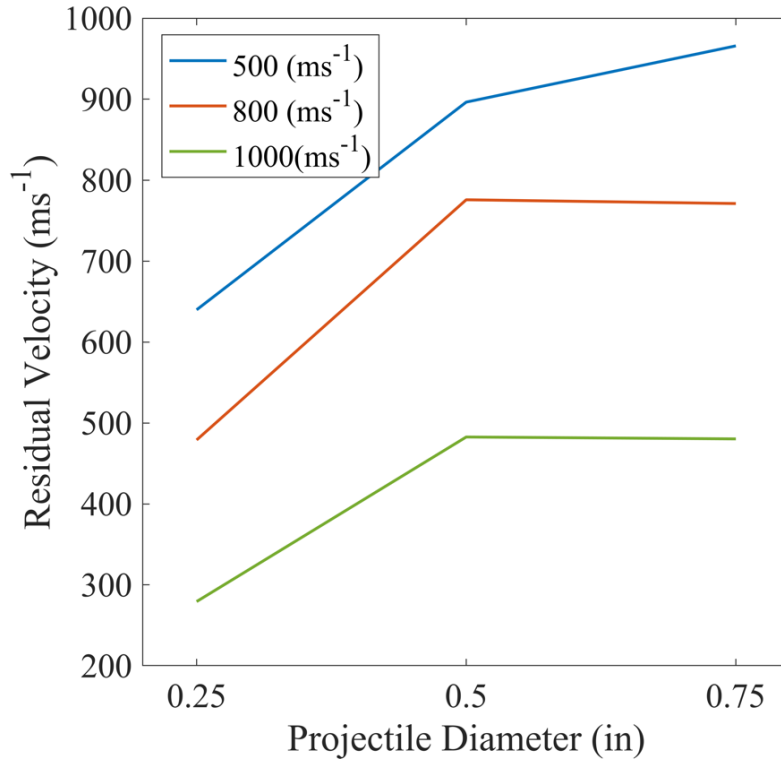


Figure 4.7 Effect of the projectile diameter on the residual velocity for a ballistic impact at 1000ms⁻¹ and a target with a thickness of 1in.

Results show a distinct difference between projectile diameters of 0.25in and 0.5in; however, the results of projectile diameters of 0.5in and 0.75in were similar. The lack of influence on the projectile diameter after 0.5in warrant further studies to understand this behavior. However, the influence of the projectile size should be considered when evaluating the performance of the material model.

CHAPTER V

DISCUSSION OF FINITE ELEMENT SIMULATION RESULTS AND FUTURE WORK

5.1 Concrete Target Fragmentation Process

Several features of the ballistic impact scenario were captured during these simulations. The ballistic impact loading scenario is a unique problem due to the complex stress states and the behavior of the stress waves throughout the contact between the projectile and concrete. The cross-sectional view of the target for a simulation with an initial velocity of 1000 ms^{-1} and target thickness of 1in is shown by Figure 5.1.

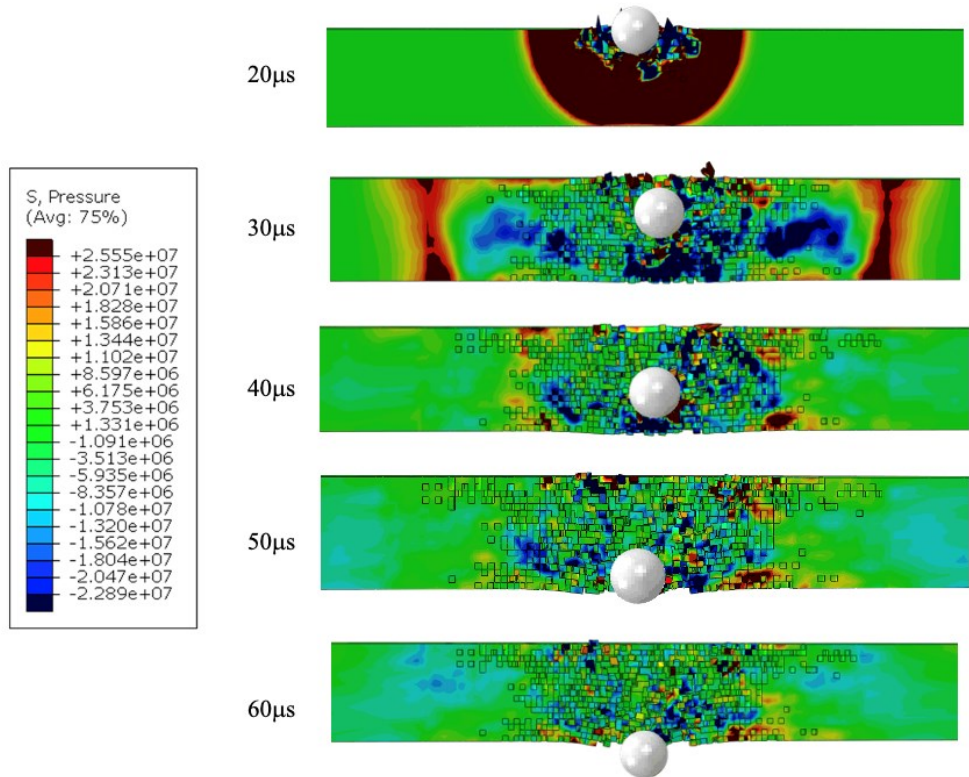


Figure 5.1 Pressure contour showing the stress wave propagation through the cross section of the target for a ballistic impact of a 1in target and a 1000ms^{-1} initial velocity.

As the projectile initiates contact with the projectile, a large spherical compressive wave is seen to propagate outward from the projectile at $20\mu\text{s}$. This initial stress wave continues to propagate outward from the projectile at $30\mu\text{s}$. These compressive pressures are transformed to tensile pressures and are seen in Figure 5.1 to trail behind the initial compressive wave. Tensile pressures are also seen to precede the projectile on the back face of the target. The initial pressure wave was seen to continue expanding radially throughout the target. Once the pressure waves contact the boundary conditions simulating the fixture supporting the concrete target, the waves reflect to the center of the target. Part of this reflection is seen between 40 and $60\mu\text{s}$ in

Figure 5.1. As previously mentioned, tensile pressures are known to cause material spalling and be the prime contributor of the material damage of concrete. Evidence of the tensile spalling seen throughout the simulations are highlighted in Figure 5.2.



Figure 5.2 Aspects of the ballistic impact seen throughout the target of a ballistic impact simulation with an initial velocity of 1000ms^{-1} and target thickness of 1in.

Figure 5.2 shows the aspects of the ballistic impact by the tunneling of the projectile, tensile spalling, and the radial cracking due to the ballistic impact. The mesal zone was also observed by the interface between the projectile and the target during the initial portions of the simulations. The tunneling of the projectile is well established in the simulations; however, there is limited evidence of radial cracking and tensile spalling. The limited evidence of radial cracking is seen in Figure 5.2 and is seen to localize near the impact site of the projectile. Additionally, the damage of the concrete target progressed radially from the impact site and its contribution to fragmentation outside of the impact zone was limited on the front and back face

in addition to its cross section. Both the scabbing and tunneling diameters were found to be larger on the rear of the target than on the front of the target. The resulting targets are shown by Figure 5.3.

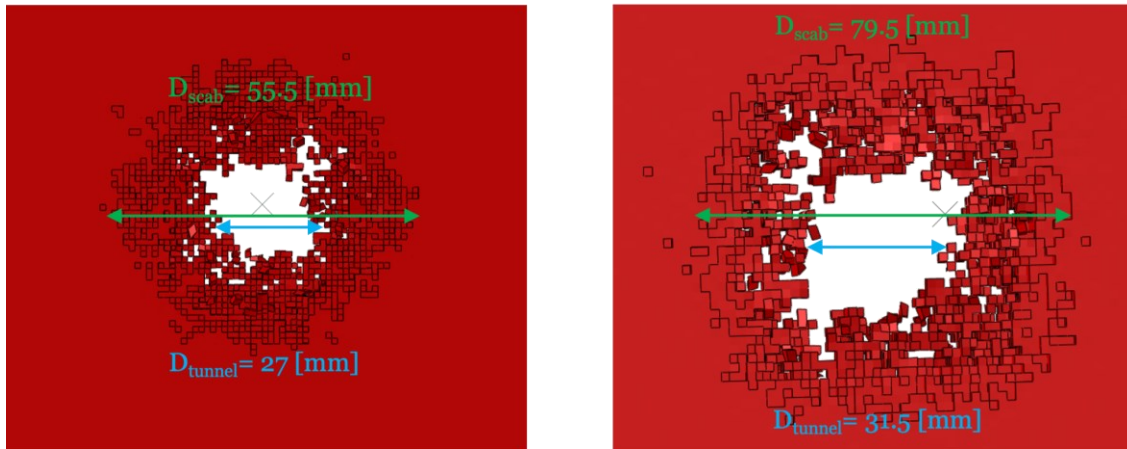


Figure 5.3 Resulting scabbing and tunnel diameters from a ballistic impact with an initial velocity of 1000ms^{-1} and target thickness of 1in.

Figures shows the damage in the finite element simulations on the front face (left) and rear face (right) of the target.

The scabbing diameter of the front side of the 1in thick target, which was impacted by an initial velocity of 1000ms^{-1} , was determined to be 55.5mm while the rear face indicated a 79.5mm scabbing diameter. Furthermore, the tunneling diameter of the front face was 27mm while the rear face was 31.5mm. Since the tensile damage is known to be the primary mechanism of fracture for concrete, it is not surprising the rear face produced greater indications of damage in the simulations. However, an increase of 4.5mm in tunneling diameter is not substantial. A qualitative assessment of the damaged targets in the simulations indicate the damage expands

radially from the impact site and any cracking patterns that propagate outward from the impact site were extremely limited in the results as previously mentioned. Strong evidence as to the effectiveness of this concrete model in its prediction of the ballistic impact can be accomplished by a qualitative comparison of the produced target craters from the simulations to experimental data.

5.2 Limitations of Finite Element Model and Future Work

The key limitation in this work, is the lack of experimental data of ballistic impacts to the BBR9 concrete to validate the performance of the CDPM2 model. However, based on the simulation results, it is expected the concrete model underrepresents the contribution of tensile damage in the ballistic impact simulations. This reasoning is due to the similarities between the damage of the front and rear face of the target and the lack of observed tensile spalling in the simulations. Experimental data and ballistic impact simulations by other researchers have produced models which capture the large contribution of tensile damage along with a high degree of spalling in the material and radial cracking (Forquin et al., 2015; Zaera and Sánchez-Gálvez, 1998). This indicates the need for improvement in the concrete material model to fully capture the effects due to high strain rate ballistic impacts.

To better represent the ballistic impact scenarios, a new damage model will be introduced to replace the damage model in CDPM2. The damage model presented in (Pereira et al., 2018b) has shown to well capture the damage effects of a high strain rate impact for concrete. It was validated through a comparison with experimental data of a ballistic impact and was found to capture the cracking and damage at both the site of impact and opposite the side of impact. Additionally, it matched well with the presented numerical results of the impact experiments.

This model includes a new damage parameter that accounts for crushing through the hydrostatic damage variable (ω_h^*). The total damage in the model is defined in terms of the tensile damage (ω_t), compressive damage (ω_c), and hydrostatic damage variables seen in equation 5.1.

$$\omega = 1 - (1 - \omega_t)(1 - \omega_c)(1 - \omega_h^*) \quad (5.1)$$

The evolution of the stress tensor (σ) shown by equation 5.2 is defined in terms of the total damage and the effective stress tensor ($\tilde{\sigma}$).

$$f(x) = \begin{cases} K_{new} = K_{el}(1 - \omega_h) + K_{solid}H_c & \text{if } \Delta\omega_h > 0 \\ K_{reload} = K_{el} + K_{solid}H_e & \text{if } \Delta\omega_h = 0 \end{cases} \quad (5.2)$$

The combination of the CDPM2 plasticity and the new damage model are expected to produce a new concrete material model, which can well predict the behavior of concrete at high strain rates. Future work will also include the validation of the new concrete material model to experimental data of ballistic impacts for BBR9 concrete.

CHAPTER VI

CONCLUSION

In this study finite element simulations were developed to predict the behavior of concrete subjected to the high strain rate loadings of ballistic impacts. The existing CDPM2 concrete material model was implemented by calibrating the model to triaxial compressive experiments of BBR9 high strength concrete. The simulations were designed to ascertain the response of concrete targets undergoing high strain rates through ballistic impacts by assessing its response at differing initial projectile velocities, different concrete target thicknesses, and different projectile sizes. The results indicated a mostly linear relationship between the initial projectile velocity and the residual velocity of the projectile. A similar trend was also seen for the residual velocities compared to different target thicknesses. The impact dynamics of the simulation were evaluated to study the different phases of the impact. The simulations captured the initial pressure wave resulting from the impact and its reflection from the constraint on the target. Certain aspects of the ballistic impact such as radial cracking, tensile spalling, and tunneling of the projectile were captured in the simulations. However, limitations in the current model were evident through the limited degree of tensile damage seen through the crater sizes in the rear face of the target. Additionally, the fragmentation of the target was found to most noticeably extend radially from the impact site and evidence of cracking throughout the target away from the impact zone was limited. Future work will include the combination of the

CDPM2 plasticity formulation and a new damage formulation to better capture the high strain rate response. Additionally, a model validation will be completed to assess the ability of the new concrete material model to predict the behavior of concrete during ballistic impacts.

REFERENCES

- ABAQUS: Theory Manual, Version 6.6, 2009.
- Alkaysi, M., El-Tawil, S., Liu, Z., Hansen, W., 2016. Effects of silica powder and cement type on durability of ultra high performance concrete (UHPC). *Cement and Concrete Composites* 66, 47–56. <https://doi.org/10.1016/j.cemconcomp.2015.11.005>
- Beppu, M., Miwa, K., Itoh, M., Katayama, M., Ohno, T., 2008. Damage evaluation of concrete plates by high-velocity impact. *International Journal of Impact Engineering, Hypervelocity Impact Proceedings of the 2007 Symposium* 35, 1419–1426. <https://doi.org/10.1016/j.ijimpeng.2008.07.021>
- Bischoff, P.H., Perry, S.H., 1991. Compressive behaviour of concrete at high strain rates. *Materials and Structures* 24, 425–450. <https://doi.org/10.1007/BF02472016>
- Bohong, G., 2004. Ballistic Penetration of Conically Cylindrical Steel Projectile into Plain-woven Fabric Target – A Finite Element Simulation [WWW Document]. URL <https://journals.sagepub.com/doi/10.1177/0021998304044776> (accessed 6.12.21).
- Chen, T., Li, Q.B., Guan, J.F., 2013. Effect of Radial Inertia Confinement on Dynamic Compressive Strength of Concrete in SHPB Tests [WWW Document]. *Applied Mechanics and Materials*. <https://doi.org/10.4028/www.scientific.net/AMM.438-439.215>
- Dou, Y., Liu, Y., Huddleston, B., Hammi, Y., Horstemeyer, M.F., 2020. A molecular dynamics study of effects of crystal orientation, size scale, and strain rate on penetration mechanisms of monocrystalline copper subjected to impact from a nickel penetrator at very high strain rates. *Acta Mech* 231, 2173–2201. <https://doi.org/10.1007/s00707-020-02632-8>
- Dou, Y., Liu, Y., Whittington, W., Miller, J., 2016. Experimental Calibration of ISV Damage Model Constants for Pure Copper for High-Speed Impact Simulation, in: *Volume 9: Mechanics of Solids, Structures and Fluids; NDE, Diagnosis, and Prognosis*. Presented at the ASME 2016 International Mechanical Engineering Congress and Exposition, American Society of Mechanical Engineers, Phoenix, Arizona, USA, p. V009T12A039. <https://doi.org/10.1115/IMECE2016-65690>
- Drucker, D.C., Prager, W., 1952. Soil mechanics and plastic analysis or limit design. *Quart. Appl. Math.* 10, 157–165. <https://doi.org/10.1090/qam/48291>

- Forquin, P., Sallier, L., Pontiroli, C., 2015. A numerical study on the influence of free water content on the ballistic performances of plain concrete targets. *Mechanics of Materials* 89, 176–189. <https://doi.org/10.1016/j.mechmat.2015.02.016>
- Gebbeken, N., Hartmann, T., 2010. A New Methodology for the Assessment of the EoS Data of Concrete. *International Journal of Protective Structures* 1, 299–317. <https://doi.org/10.1260/2041-4196.1.3.299>
- Grassl, P., Jirásek, M., 2006. Damage-plastic model for concrete failure. *International Journal of Solids and Structures* 43, 7166–7196. <https://doi.org/10.1016/j.ijsolstr.2006.06.032>
- Grassl, P., Johansson, M., Leppänen, J., 2018. On the numerical modelling of bond for the failure analysis of reinforced concrete. *Engineering Fracture Mechanics* 189, 13–26. <https://doi.org/10.1016/j.engfracmech.2017.10.008>
- Grassl, P., Xenos, D., Nystrom, U., Rempling, R., Gylltoft, K., 2013. CDPM2: A damage-plasticity approach to modelling the failure of concrete. *International Journal of Solids and Structures* 50, 3805–3816. <https://doi.org/10.1016/j.ijsolstr.2013.07.008>
- Grote, D.L., Park, S.W., Zhou, M., 2001. Dynamic behavior of concrete at high strain rates and pressures: I. experimental characterization. *International Journal of Impact Engineering* 25, 869–886. [https://doi.org/10.1016/S0734-743X\(01\)00020-3](https://doi.org/10.1016/S0734-743X(01)00020-3)
- Hai, L., Ren, X., 2020. Computational investigation on damage of reinforced concrete slab subjected to underwater explosion. *Ocean Engineering* 195, 106671. <https://doi.org/10.1016/j.oceaneng.2019.106671>
- He, G., Dou, Y., Guo, X., Liu, Y., 2018a. Computational Investigation of Effects of Grain Size on Ballistic Performance of Copper. *International Journal for Computational Methods in Engineering Science and Mechanics* 19, 1–10. <https://doi.org/10.1080/15502287.2017.1370510>
- He, Ge, Dou, Y., Guo, X., Liu, Y., 2017. Effects of Grain Size on Ballistic Response of Copper Materials, in: *Volume 14: Emerging Technologies; Materials: Genetics to Structures; Safety Engineering and Risk Analysis*. Presented at the ASME 2017 International Mechanical Engineering Congress and Exposition, American Society of Mechanical Engineers, Tampa, Florida, USA, p. V014T11A004. <https://doi.org/10.1115/IMECE2017-70585>
- He, G., Liu, Y., 2019. Theoretical Modeling of the Mechanical Degradation of Polymer Composites due to Moisture/Water Absorption and Damage Progression. Presented at the AeroTech Americas, pp. 2019-01–1376. <https://doi.org/10.4271/2019-01-1376>

- He, G., Liu, Y., Bammann, D.J., Francis, D.K., Chandler, M.Q., Horstemeyer, M.F., 2019a. A multiphase internal state variable model with rate equations for predicting elastothermoviscoplasticity and damage of fiber-reinforced polymer composites. *Acta Mech* 230, 1745–1780. <https://doi.org/10.1007/s00707-018-2358-1>
- He, G., Liu, Y., Bammann, D.J., Horstemeyer, M.F., 2018b. An Elastothermoviscoplasticity Anisotropic Damage Model for Short Fiber Reinforced Polymer Composites, in: Volume 12: Materials: Genetics to Structures. Presented at the ASME 2018 International Mechanical Engineering Congress and Exposition, American Society of Mechanical Engineers, Pittsburgh, Pennsylvania, USA, p. V012T11A036. <https://doi.org/10.1115/IMECE2018-86286>
- He, G., Liu, Y., Deng, X., Fan, L., 2019b. Constitutive modeling of viscoelastic–viscoplastic behavior of short fiber reinforced polymers coupled with anisotropic damage and moisture effects. *Acta Mech. Sin.* 35, 495–506. <https://doi.org/10.1007/s10409-018-0810-z>
- He, G., Liu, Y., Hammi, Y., Bammann, D.J., Horstemeyer, M.F., 2020. A combined viscoelasticity-viscoplasticity-anisotropic damage model with evolving internal state variables applied to fiber reinforced polymer composites. *Mechanics of Advanced Materials and Structures* 1–22. <https://doi.org/10.1080/15376494.2019.1709673>
- He, G., Liu, Y., Horstemeyer, M., Bammann, D., 2017. A multiphase internal state variable model for predicting the plasticity and damage mechanisms of fiber-reinforced polymers. Presented at the IMECE2017, Tampa, FL, USA.
- He, G., Liu, Y., Lacy, T.E., Horstemeyer, M.F., 2021. A historical review of the traditional methods and the internal state variable theory for modeling composite materials. *Mechanics of Advanced Materials and Structures* 1–22. <https://doi.org/10.1080/15376494.2021.1872124>
- Jiang, J.-F., Wu, Y.-F., 2012. Identification of material parameters for Drucker–Prager plasticity model for FRP confined circular concrete columns. *International Journal of Solids and Structures* 49, 445–456. <https://doi.org/10.1016/j.ijsolstr.2011.10.002>
- Katayama, M., Abe, A., Takeba, A., 2017. Investigation on Mie-Grüneisen type shock Hugoniot equation of state for concrete | *The International Journal of Multiphysics*.
- Knoeri, C., Sanyé-Mengual, E., Althaus, H.-J., 2013. Comparative LCA of recycled and conventional concrete for structural applications. *Int J Life Cycle Assess* 18, 909–918. <https://doi.org/10.1007/s11367-012-0544-2>
- Leutbecher, T., n.d. Design relevant properties of hardened Ultra High Performance Concrete 12.

- Li, Q.M., Meng, H., 2003. About the dynamic strength enhancement of concrete-like materials in a split Hopkinson pressure bar test. *International Journal of Solids and Structures* 40, 343–360. [https://doi.org/10.1016/S0020-7683\(02\)00526-7](https://doi.org/10.1016/S0020-7683(02)00526-7)
- Li, Q.M., Reid, S.R., Wen, H.M., Telford, A.R., 2005. Local impact effects of hard missiles on concrete targets. *International Journal of Impact Engineering*, Fifth International Symposium on Impact Engineering 32, 224–284. <https://doi.org/10.1016/j.ijimpeng.2005.04.005>
- Li, Q.M., Tong, D.J., 2003. Perforation Thickness and Ballistic Limit of Concrete Target Subjected to Rigid Projectile Impact. *Journal of Engineering Mechanics* 129, 1083–1091. [https://doi.org/10.1061/\(ASCE\)0733-9399\(2003\)129:9\(1083\)](https://doi.org/10.1061/(ASCE)0733-9399(2003)129:9(1083))
- Liu, Y., Chu, S., Viera, R., 2011. Analysis of Structural Impact and Crashworthiness using Experimental, Analytical and Computational Techniques: An Overview and Recent Developments. *Int. J. Vehicle Structures & Systems* 3. <https://doi.org/10.4273/ijvss.3.3.01>
- Liu, Y., Day, M., 2006. Impact experimental analysis and computer simulation using ANSYS. Presented at the 2006 International ANSYS Conference, Pittsburgh, PA, USA.
- Liu, Y., Day, M.L., 2008. Experimental Analysis and Computer Simulation of Automotive Bumper System under Impact Conditions. *International Journal for Computational Methods in Engineering Science and Mechanics* 9, 51–59. <https://doi.org/10.1080/15502280701759218>
- Liu, Y., Dou, Y., Hammi, Y., 2015a. Computational Investigation of High Velocity Penetration of Copper Subjected to Impact From Nickel Projectiles, in: *Volume 9: Mechanics of Solids, Structures and Fluids*. Presented at the ASME 2015 International Mechanical Engineering Congress and Exposition, American Society of Mechanical Engineers, Houston, Texas, USA, p. V009T12A003. <https://doi.org/10.1115/IMECE2015-50241>
- Liu, Y., Dou, Y., Justin, W., Horstemeyer, S.J., Thirumalai, R.V.K.G., Williams, W., 2015b. Experimental Study of High Velocity Penetration of an Aluminum Target Plate by a Spherical Projectile, in: *Volume 9: Mechanics of Solids, Structures and Fluids*. Presented at the ASME 2015 International Mechanical Engineering Congress and Exposition, American Society of Mechanical Engineers, Houston, Texas, USA, p. V009T12A028. <https://doi.org/10.1115/IMECE2015-50243>
- Luccioni, B., Isla, F., Codina, R., Ambrosini, D., Zerbino, R., Giaccio, G., Torrijos, M.C., 2018. Experimental and numerical analysis of blast response of High Strength Fiber Reinforced Concrete slabs. *Engineering Structures* 175, 113–122. <https://doi.org/10.1016/j.engstruct.2018.08.016>

- Mainstone, R.J., 1975. Properties of materials at high rates of straining or loading. *Mat. Constr.* 8, 102–116. <https://doi.org/10.1007/BF02476328>
- Mao, L., Barnett, S., Begg, D., Schleyer, G., Wight, G., 2014. Numerical simulation of ultra high performance fibre reinforced concrete panel subjected to blast loading. *International Journal of Impact Engineering* 64, 91–100. <https://doi.org/10.1016/j.ijimpeng.2013.10.003>
- Martineau, R.L., 1998. A viscoplastic model of expanding cylindrical shells subjected to internal explosive detonations (No. LA--13424-T, 663184). <https://doi.org/10.2172/663184>
- Pereira, L.F., Weerheijm, J., Sluys, L.J., 2018a. Simulation of compaction and crushing of concrete in ballistic impact with a new damage model. *International Journal of Impact Engineering* 111, 208–221. <https://doi.org/10.1016/j.ijimpeng.2017.09.014>
- Pereira, L.F., Weerheijm, J., Sluys, L.J., 2018b. Simulation of compaction and crushing of concrete in ballistic impact with a new damage model. *International Journal of Impact Engineering* 111, 208–221. <https://doi.org/10.1016/j.ijimpeng.2017.09.014>
- Pontioli, C., 2019. Impact response of UHPC and UHPFRC: experimental study and numerical simulation, in: *Proceedings of the 10th International Conference on Fracture Mechanics of Concrete and Concrete Structures*. Presented at the 10th International Conference on Fracture Mechanics of Concrete and Concrete Structures, IA-FraMCoS. <https://doi.org/10.21012/FC10.236361>
- Russell, H., Graybeal, B., 2013. *Ultra-High Performance Concrete: A State-of-the-Art Report for the Bridge Community*.
- Seok, S., Haikal, G., Ramirez, J.A., Lowes, L.N., Lim, J., 2020. Finite element simulation of bond-zone behavior of pullout test of reinforcement embedded in concrete using concrete damage-plasticity model 2 (CDPM2). *Engineering Structures* 221, 110984. <https://doi.org/10.1016/j.engstruct.2020.110984>
- Song, P.S., Hwang, S., 2004. Mechanical properties of high-strength steel fiber-reinforced concrete. *Construction and Building Materials* 18, 669–673. <https://doi.org/10.1016/j.conbuildmat.2004.04.027>
- Soroushian, P., Choi, K.-B., Fu, G., 1985. Tensile Strength of Concrete at Different Strain Rates. *MRS Proc.* 64, 87. <https://doi.org/10.1557/PROC-64-87>
- Wille, K., Naaman, A.E., El-Tawil, S., n.d. *Optimizing Ultra-High- Performance Fiber-Reinforced Concrete* 7.
- Williams, B., Heard, W., Graham, S., Nie, X., 2020. Effect of specimen geometry on triaxial compressive response of high-strength concrete. *Construction and Building Materials* 244, 118348. <https://doi.org/10.1016/j.conbuildmat.2020.118348>

- Woodward, R.L., Baxter, B.J., Pattie, S.D., McCARTHY, P., 1991. IMPACT FRAGMENTATION OF BRITTLE MATERIALS. *J. Phys. IV France* 01, C3-259-C3-264. <https://doi.org/10.1051/jp4:1991336>
- Wu, H., Li, Y.C., Fang, Q., Peng, Y., 2019. Scaling effect of rigid projectile penetration into concrete target: 3D mesoscopic analyses. *Construction and Building Materials* 208, 506–524. <https://doi.org/10.1016/j.conbuildmat.2019.03.040>
- Yoo, D.-Y., Banthia, N., 2016. Mechanical properties of ultra-high-performance fiber-reinforced concrete: A review. *Cement and Concrete Composites* 73, 267–280. <https://doi.org/10.1016/j.cemconcomp.2016.08.001>
- Yu, T., Teng, J.G., Wong, Y.L., Dong, S.L., 2010. Finite element modeling of confined concrete-I: Drucker–Prager type plasticity model. *Engineering Structures* 32, 665–679. <https://doi.org/10.1016/j.engstruct.2009.11.014>
- Yun, S.-H., Park, T., 2013. Multi-physics blast analysis of reinforced high strength concrete. *KSCE J Civ Eng* 17, 777–788. <https://doi.org/10.1007/s12205-013-0093-7>
- Zaera, R., Sánchez-Gálvez, V., 1998. Analytical modelling of normal and oblique ballistic impact on ceramic/metal lightweight armours. *International Journal of Impact Engineering* 21, 133–148. [https://doi.org/10.1016/S0734-743X\(97\)00035-3](https://doi.org/10.1016/S0734-743X(97)00035-3)
- Zhang, M., Wu, H.J., Li, Q.M., Huang, F.L., 2009. Further investigation on the dynamic compressive strength enhancement of concrete-like materials based on split Hopkinson pressure bar tests. Part I: Experiments. *International Journal of Impact Engineering, Seventh International Conference on Shock and Impact Loads on Structures* 36, 1327–1334. <https://doi.org/10.1016/j.ijimpeng.2009.04.009>

ProQuest Number: 28720676

INFORMATION TO ALL USERS

The quality and completeness of this reproduction is dependent on the quality and completeness of the copy made available to ProQuest.



Distributed by ProQuest LLC (2021).

Copyright of the Dissertation is held by the Author unless otherwise noted.

This work may be used in accordance with the terms of the Creative Commons license or other rights statement, as indicated in the copyright statement or in the metadata associated with this work. Unless otherwise specified in the copyright statement or the metadata, all rights are reserved by the copyright holder.

This work is protected against unauthorized copying under Title 17, United States Code and other applicable copyright laws.

Microform Edition where available © ProQuest LLC. No reproduction or digitization of the Microform Edition is authorized without permission of ProQuest LLC.

ProQuest LLC
789 East Eisenhower Parkway
P.O. Box 1346
Ann Arbor, MI 48106 - 1346 USA